

THESIS

**A Study of Baseline Compensation
System for Stable Operation of
Gravitational-wave Telescope**

Koseki Miyo

*Department of Physics
University of Tokyo*

MMM 2020

Abstract

a

要旨

2015 年、ブラックホール連星合体からの重力波 GW150914 を LIGO の 2 台の検出器が直接検出することに成功した。また 2017 年には Virgo を加えた 3 台の重力波検出器で連星中性子合体からの重力波 GW170817 を検出し、さらにフォローアップ観測によって電磁波対応天体も同定され、マルチメッセンジャー観測が確立された。そして 2020 年には KAGRA も LIGO と Virgo の重力波観測ネットワークに加わることで、より多くの重力波イベントの観測が期待される。

しかしながら、重力波は地球のどこでも検出できて視界に左右されないはずだが、現在稼働している干渉計型重力波検出器の DutyCycle は 60 % 程度である。これは悪天候時の高波や遠地でおきた地震などによる地面振動によって、干渉計の腕が変動し、干渉しなくなるためである。これら地面振動はおよそ 1 Hz 以下で数 10 km 以上のスケールで地面を揺らすが、現状の防振装置ではこのような低周波地面振動は防振できない。これは、グローバルな低周波の地面揺れを測定できるセンサーがないためである。

本論文では、基線長補償システムについて書かれている。このシステムは、レーザーひずみ計と呼ばれる地殻変動計測用の 1.5 km のレーザー干渉計をもちいて KAGRA の基線長伸縮をモニターし、その信号で、メインの KAGRA の干渉計が揺れないように防振をする。

この論文では、地面振動が干渉計に与える影響について調べられており、そしてその影響を低減するための基線長補償システムの原理と、その理論的性能、既存のシステムと比較した利点が調べられている。そして、このシステムを実際に KAGRA に組み込んだ性能評価実験が述べられている。この実験では、もっとも地面振動の影響を受けやすい 3 km の Fabry-Perot 光共振器に基線長補償システムを組み込み、この腕共振器の長さ変動を測定した。その結果、

Contents

Abstract	3
要旨	5
1 Seismic Noise	11
1.1 Theory of seismic waves	12
1.1.1 Seismic Waves	12
1.1.2 Reduction Effect of the Short Baseline	14
1.2 Seismic Noise	17
1.2.1 Cultural Noises	19
1.2.2 Natural Noises	19
1.3 Study of Seismic Noise of KAGRA Mine	22
1.3.1 Overview	22
1.3.2 Experimental Arrangement	22
1.3.3 Data Processing	23
1.3.4 Study of Long-term Seismic Noise	24
1.3.5 Study of the Differential Motion Reduction	26
1.4 Summary of the Chapter	26

Chapter 1

Seismic Noise

Seismic noise causes two issues for laser interferometric gravitational-wave detectors; (1) limitation of the low-frequency sensitivity of the detectors and (2) deterioration of the duty cycle of that. The seismic noise above 1 Hz, which is associated with anthropogenic activity, contaminates the low-frequency sensitivity. The seismic motion below this frequency, which is generated by the natural noise source such as the ocean, disturbs the Fabry-Perot arm cavity to resonate stably.

In order to resolve these issues, a laser interferometer gravitational wave antenna with a baseline length of 20 m (LISM) [22] is constructed underground, because the low-level seismic noise is expected in the underground environment. As a result, the seismic noise in LISM site is less than that in the surface site by two orders of magnitude in 1–100 Hz region, and the underground GW detector performed stable operation with duty cycle of 99.8%.

However, for km-meter scale GW detector like KAGRA, such a stable operation can not be expected because

- length of the long baseline is susceptible to the low-frequency seismic motion compared with the short one due to the a few reduction effect kind of the *common mode rejection*, and this problem is common in not only all the current detectors but also the next 10 km-scale detectors; Einstein Telescope (ET)[36] and Cosmic Explorer (CE) [37].

- especially in KAGRA site, the microseismic noise correlated with the ocean activity in 0.03–0.3 Hz, which is the most problematic noise for stable operation of GW detector, cannot be reduced even in the underground due to near the sea (40 km from Toyama Bay), and this problem is common in ET which is also will be constructed in underground but in island [38].

The purpose of this chapter is to describe quantitatively above two problems. In this chapter, first, section 1.1 gives an theoretical understanding of the seismic noise as the elastic waves. In section 1.2, some general properties of the seismic noise are described by quoting previous researches. Finally, we discuss the problems in section 1.3.

1.1 Theory of seismic waves

Here we introduce characteristics of the seismic wave that will be usefull in our later understanding and modeling of seismic effects.

1.1.1 Seismic Waves

The elastodynamic wave equation without external forces is given by

$$\rho \ddot{\mathbf{u}} = (\lambda + 2\mu) \nabla(\nabla \cdot \mathbf{u}) - \mu \nabla \times (\nabla \times \mathbf{u}), \quad (1.1)$$

where \mathbf{u} is the displacement field vector of the medium, ρ denotes density of the medium, and λ, μ are Lamé's first and second parameter.

Body Waves

From Eq.(1.1), we can obtain two characteristic waves; longitudinal wave (primary wave, P-wave) and transverse wave (secondary wave, S-wave). First, using Helmholtz's decomposition, we represent the displacement field vector \mathbf{u} as

$$\mathbf{u} = \nabla \phi + \nabla \times \boldsymbol{\psi}, \quad (1.2)$$

where ϕ the scalar potential and $\boldsymbol{\psi}$ are the vector potential. Each term of Eq.(1.2) show the divergent and the rotation component of \mathbf{u} respectively. Substitute

Eq.(1.2) into Eq.(1.1) and after some vector algebra, one can obtain two wave equations;

$$\ddot{\phi} = v_L^2 \nabla^2 \phi, \quad (1.3)$$

$$\ddot{\psi} = v_T^2 \nabla^2 \psi, \quad (1.4)$$

where v_L, v_T are defined as

$$v_L = \sqrt{\frac{\lambda + 2\mu}{\rho}}, \quad v_T = \sqrt{\frac{\mu}{\rho}}. \quad (1.5)$$

These phase velocities; v_L, v_T represent that of the P-wave and the S-wave. Show this relationships. Because the scalar potential and the vector potential are obey the wave equation Eq.(1.3) and Eq.(1.4) respectively, the general solutions of these potentials are given as

$$\phi = \phi_0(\omega t - \mathbf{k} \cdot \mathbf{x}) \quad (1.6)$$

$$\psi = \psi_0(\omega t - \mathbf{k} \cdot \mathbf{x}), \quad (1.7)$$

where ω, \mathbf{k} are the angular frequency and the wave vector. One can obtain the divergent component of displacement field vector \mathbf{u} as

$$\mathbf{u}_{\text{div}} = \nabla \phi_0(\omega t - \mathbf{k} \cdot \mathbf{x}) = -\mathbf{k} \phi. \quad (1.8)$$

The displacement of this wave \mathbf{u}_{div} whose phase velocity is v_L propagates along with direction of the wave vector. Therefore v_L is the phase velocity of a longitudinal wave called P-wave. On the other hands, one can obtain the rotation component of \mathbf{u} as

$$\mathbf{u}_{\text{rot}} = \nabla \times \psi_0(\omega t - \mathbf{k} \cdot \mathbf{x}) = -\mathbf{k} \times \psi. \quad (1.9)$$

This displacement vector \mathbf{u}_{rot} whose phase velocity is v_T is perpendicular to the wave vector. Therefore, v_T is the phase velocity of a transverse wave called S-wave. Furthermore, because λ and μ are positive numbers,

$$v_L > v_T. \quad (1.10)$$

Therefore, the longitudinal wave is faster than the transverse wave.

Rayleigh waves

Rayleigh wave is produced by the interfer of P-wave and S-Wave [39].

Rayleigh wave は P 波と S 波の干渉によって生じる [39]。ここでは Z 軸を鉛直方向とした直交直線座標系の x-z 面内で振動する弾性波を考える。z=0 を自由表面とし、x 軸に沿って P 波と S 波が同じ速度 $v_R = \omega/k$ (ω is angular frequency and k is the wave vector) で伝搬する場合を考えると、ポテンシャル ϕ と ψ は、それぞれ以下のように表すことができる。

$$\phi = F(z) \exp[i(kx - \omega t)], \quad (1.11)$$

$$\psi = G(z) \exp[i(kx - \omega t)] \quad (1.12)$$

Eq.1.11 と Eq.1.12 を波動方程式 Eq.1.3, Eq.1.4 に代入すれば、レイリー波の特性方程式が導かれる;

$$\left(\frac{c_R^2}{c_S^2}\right)^3 - 8\left(\frac{c_R^2}{c_S^2}\right)^2 + 8\left(3 - \frac{2}{\gamma^2}\right)\left(\frac{c_R^2}{c_S^2}\right) - 16\left(1 - \frac{1}{\gamma^2}\right) = 0 \quad (1.13)$$

where $\gamma \equiv v_L/v_T$. In case that $0 < (\frac{c_R^2}{c_S^2}) < 1$, the velocity has physically meaningful value. According to Eq.1.13, the ratio $\frac{c_R}{c_S}$ is a function of the ratio of γ . たとえば、KAGRA と同じ山の下に建設された 100m の重力波望遠鏡 CLIO での P 波と S 波の位相速度はそれぞれ AA、BB である [40] ので、 $\gamma = 1.82$ である。したがってこのときのレイリー波の位相速度は CC である。

1.1.2 Reduction Effect of the Short Baseline

For interferometric gravitational-wave detectors which need a precise length control of the optical resonate cavity, it is appropriate to consider about the relative displacement between two points rather than the displacement of single point.

Differential Motion and Common Motion

We define the motion of two points shown in Fig.(1.1) as $\mathbf{u}_1 = \mathbf{u}(t, \mathbf{x}_1)$ and $\mathbf{u}_2 = \mathbf{u}(t, \mathbf{x}_2)$, respectively. The motions of the two points can be represented as the differential motion and the common motion. The displacement of both

differential motion and common motion of the two points shown in Fig.(1.1) are defined as

$$\mathbf{u}_{\text{diff}} \equiv \frac{\mathbf{u}_1 - \mathbf{u}_2}{\sqrt{2}}, \quad (1.14)$$

$$\mathbf{u}_{\text{comm}} \equiv \frac{\mathbf{u}_1 + \mathbf{u}_2}{\sqrt{2}} \quad (1.15)$$

These two motions defined in Eq.(1.14) and Eq.(1.15) are normalized by $\sqrt{2}$ to conserve the total power.

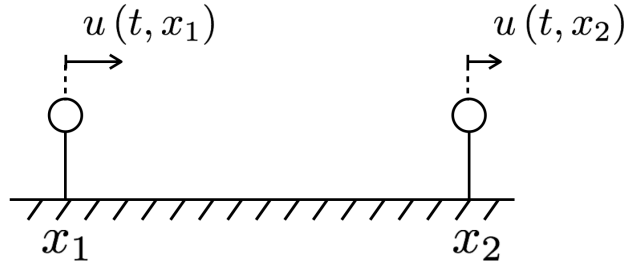


Figure 1.1: The displacements of the two points which are separated L in X axis. $\mathbf{u}(t, \mathbf{x})$ is the displacement field vector, where t denotes the time and \mathbf{x} denotes the location vector.

Common and Differential Motion Ratio (CDMR)

We define the power ratio of the common motion over the differential motion as common and differential motion ratio (CDMR). This ratio is useful to describe how the differential motion is reduced in the baseline compared to the common motion. CDMR is defined as

$$\text{CDMR} \equiv \sqrt{\frac{\text{Common Motion}}{\text{Differential Motion}}} = \sqrt{\frac{P_{\text{comm}}(\omega)}{P_{\text{diff}}(\omega)}} \quad (1.16)$$

where $P_{\text{comm}}, P_{\text{diff}}$ are the power spectral densities (PSDs) of the differential motion and common motion, respectively. In order to obtain these PSDs, we convert

from the autocorrelation function of these. Therefore, first, autocorrelation function C_{diff} of the differential motion is given by its definition in Eq.(1.15)

$$C_{\text{diff}}(\tau) = \frac{1}{2} \left\langle \left[x_1(t) - x_2(t) \right] \left[x_1(t + \tau) - x_2(t + \tau) \right] \right\rangle \quad (1.17)$$

$$= \frac{1}{2} \left[C_{11}(\tau) - C_{12}(\tau) - C_{21}(\tau) + C_{22}(\tau) \right], \quad (1.18)$$

,where C_{ij} are the autocorrelation functions of each point and defined as $C_{ij} \equiv \langle x_i(t)x_j(t + \tau) \rangle$, ($i = 1, 2, j = 1, 2$). Here, one can obtain the power spectrum density of differential motion $P_{\text{diff}}(\omega)$ as

$$P_{\text{diff}}(\omega) = \frac{1}{2} \left[P_1(\omega) + P_2(\omega) - P_{12}(\omega) - P_{12}^*(\omega) \right] \quad (1.19)$$

$$= \frac{1}{2} \left[P_1 + P_2 - \text{Re}[\gamma] \times 2\sqrt{P_1 P_2} \right], \quad (1.20)$$

where $P_1(\omega), P_2(\omega)$ are the power spectrum densities of each points, and $P_{12}(\omega)$ are the cross spectrum between two point. The parameter γ is the complex coherence between them defined by

$$\gamma \equiv \frac{P_{12}}{\sqrt{P_1 P_2}}. \quad (1.21)$$

Furthermore, assuming that seismic wave propagating each points does not decay, which means $P_1 = P_2 \equiv P$, one can compute the $P_{\text{diff}}(\omega)$ as

$$P_{\text{diff}}(\omega) = P(1 - \text{Re}[\gamma]). \quad (1.22)$$

Similarly, the PSD of the common motion can be calculated as

$$P_{\text{comm}}(\omega) = P(1 + \text{Re}[\gamma]). \quad (1.23)$$

Finally, CDMR defined Eq.(1.16) in case the seismic wave does not decay is represented as

$$\text{CDMR} = \sqrt{\frac{1 + \text{Re}[\gamma]}{1 - \text{Re}[\gamma]}}. \quad (1.24)$$

Eq.(1.24) indicates that CDMR can be expressed by only the coherence γ between of two points. For example, CDMR tends to be larger when γ close to 1. This means that the differential motion is more less than the common motion because the two points move together in the same direction.

Uniform Plane Wave Model

Consider the CDMR when the plane waves are distributed uniformly around the azimuth. Because the coherence that the single plane wave propagating with the azimuth angle θ along the direction of arm cavity from x_1 to x_2 in Fig.(1.1) is

$$\gamma = e^{i \frac{L \cos \theta \omega}{c}}, \quad (1.25)$$

the coherence in case that the plane waves propagats uniformly is given by the integral of Eq.(1.25) over all direction;

$$\gamma = \frac{1}{2\pi} \int_{-\pi}^{\pi} e^{i \frac{\omega}{c} L \cos \theta} d\theta. \quad (1.26)$$

where the coherence is normized azimuth angle. Therefore, the CDMR is given as

$$\text{CDMR} = \sqrt{\frac{1 + J_0\left(\frac{L\omega}{c}\right)}{1 - J_0\left(\frac{L\omega}{c}\right)}}. \quad (1.27)$$

For later discussion in 1.3.5, the PSD of the differential motion in case of the uniform seismic waves is usefull and is given as

$$P_{\text{diff}}(\omega) = P \left[1 - J_0 \left(\frac{L\omega}{c} \right) \right]. \quad (1.28)$$

1.2 Seismic Noise

Here we describe the actual seismic noise. Characteristics of the seismic noise are related with its origin spatially and temporally. The noise sources are spreaded anywhere; foot steps, traffics and ocean waves, and these amplitude depends on day-night or weather condition.

As summarized in Table 1.2, the seismic noises above 1 Hz are cleary correlated with cultural activities, and that below this frequency are excited by the natural phenomena [41].

This boundary frequency between cultural or natural is depends on the soil structure. At the sediment site such as the LIGO[42] and Virgo site[43], the

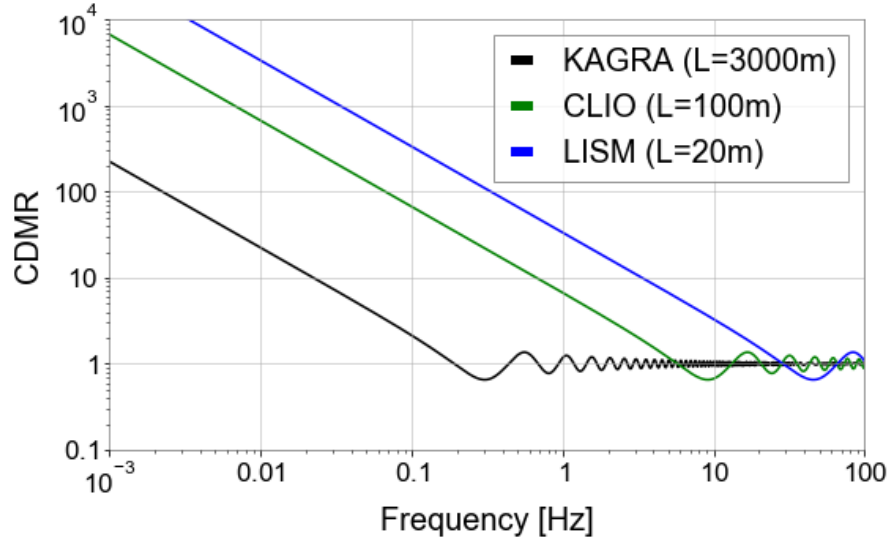


Figure 1.2: CDMR, which is the power ratio of the common motion over the differential motion of baseline in Eq.(1.27), of the underground GW detectors assuming the uniform plane waves model with phase velocity of 3000 m/sec. Black is KAGRA with the 3000 m baseline, green is CLIO with the 100 m baseline, and blue is LISM with the 20 m baseline. The CDMR of the long baseline is worse than that of short baseline. For example, at 0.1 Hz, if the baseline length is longer, the CDMR is larger..

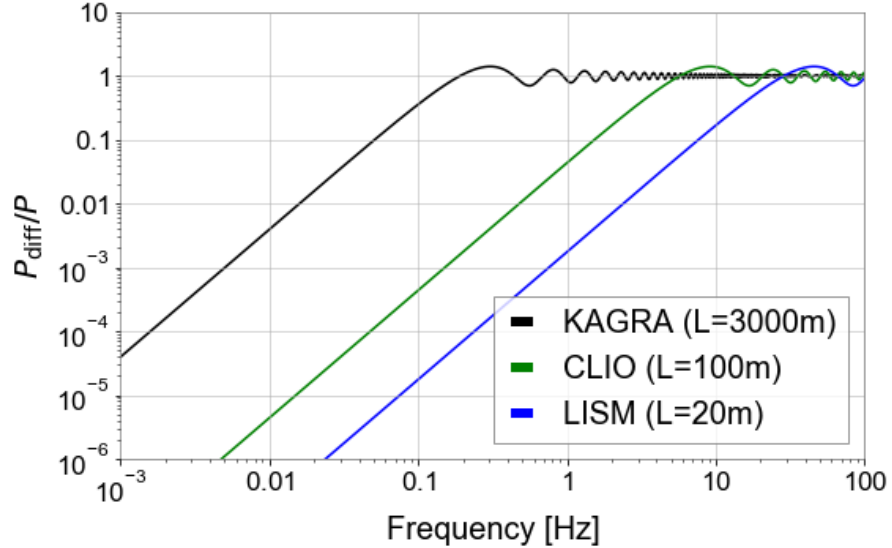


Figure 1.3: The power ratio of the differential motion of the baseline over the motion at single point; P_{diff}/P of Eq.(1.28). This ratio gives the estimation of the PSD of baseline length fluctuation from the

Table 1.1: Two types of seismic noise

Type of noise	Frequency Band	Sources
Cultural Noise	> 1 Hz	wind, traffic, machinaries, foot steps
Natural Noise	< 1 Hz	ocean, air pressure, earth tides

cultural noise can be shifted to a lower frequency and appear below 1 Hz. On the other hands, at the hard rock site such as KAGRA site, the cultural noise can be distinguished from the natural noise for its diurnal variability and apparent only above 1 Hz.

1.2.1 Cultural Noises

The cultural seismic noise contaminates the sensitivity of gravitational-wave detectors in the frequency range of interest for gravitational-waves sources, above 1 Hz. In this frequency band, the cultural noise is dominated by winds or human activities. For example, seismic noise from traffic near the detectors is reported at LIGO site [44], and noise from the vibrations of building excited by winds is reported at Virgo site [45].

1.2.2 Natural Noises

The natural seismic noise affects the stability of the GW detectors below 1 Hz because it deforms largely the ground on which mounted the detectors.

これら natural seismic noise は場所によって大きく異なることが知られている。Peterson らによって行われた、世界の 75 箇所の基地にある地震計の数年分のデータから得た地面振動のノイズスペクトルを Figure 1.4 に黒線で示す。200 mHz のピークは

Microseisms

Microseisms which power spectrum has peaks in 50–200 mHz are excited by oceanic waves. These seismic waves can be categorized by the generating mech-

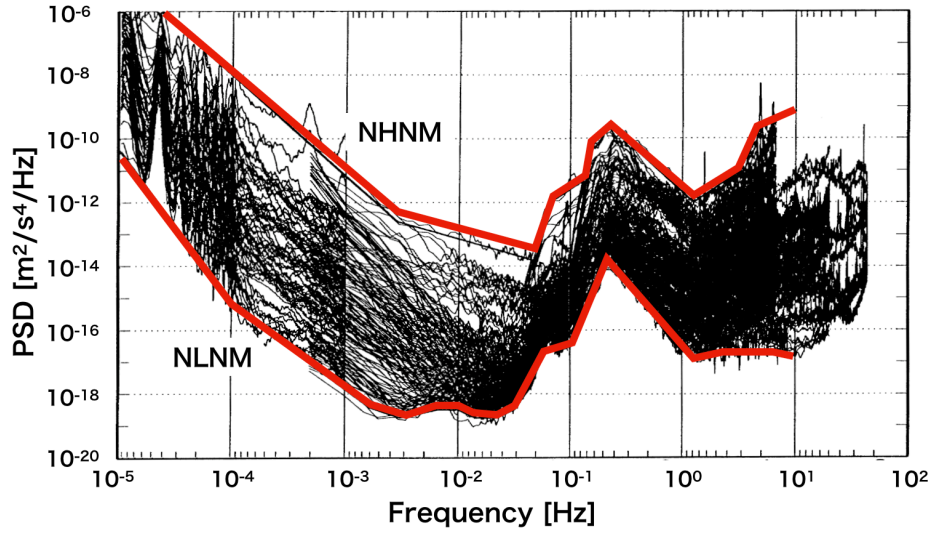


Figure 1.4: PSDs of the seismic noise obtained by Peterson in 75 stations in the world [46]. Each of the black solid lines is PSD divided into 5 different frequency band at the each stations. Each red lines are the new high noise model (NHNM) and the new low noise model (NLNM), respectively. The NHNM a spectrum of average high background noise power in the seismometer network, and the primary contributions to NHNM are inland stations situated on soft solid in very noisy locations and coastal stations with high amplitude microseisms. The NLNM represents the seismic noise when microseismic is quiet, and below microseismic, it represents the global seismic noise floor[47].

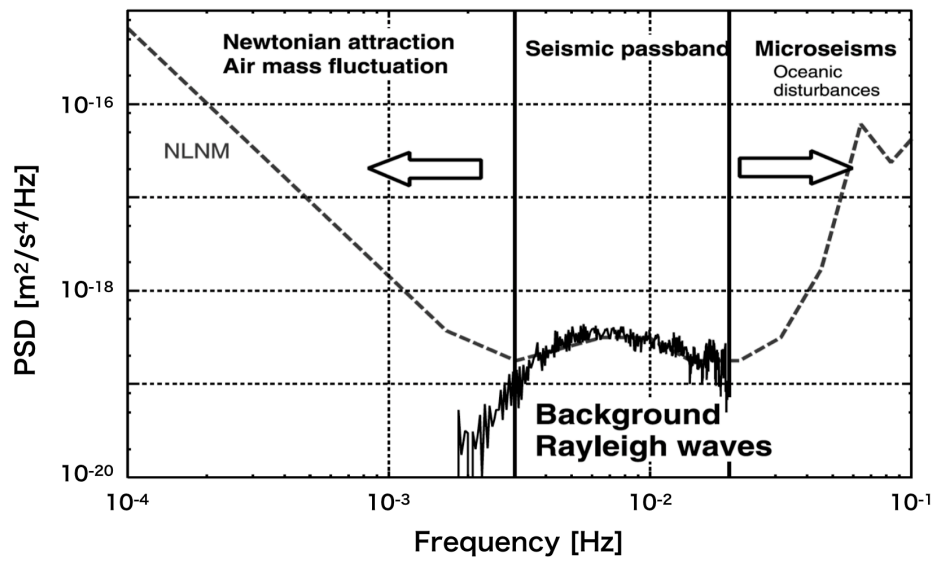


Figure 1.5: [47] から転載。

anism of these [48]. First, the primary ocean microseisms are generated only in shallow waters in coastal regions. In this regions, the water wave enery can be converted directly into seismic energy either through vertical water pressure variations, or by the impacts of surf on the shores. There are correlation between this microseismic peak and the swell at the beaches was known starting from the data sets studied by [49]. Second, the secondary ocean microseisms could be explained by the superposition of ocean waves of equal period traveling in opposite directions. Therefore, generating standing gravity waves of half the period [50].

The RMS amplitude spectral of both type of the microseisms are strongly depends on the low pressure on the ocean [38].

Seismic Noise Below 20 mHz

Below the microseismic frequency band, the main seismic noise source is an atmospheric pressure change; Rayleigh waves excited by air fluctuation on the surface, and the deformation of the Earth's crust caused by the Newtonian attraction of air mass fluctuation [51, 52]. Fig. 1.5 shows PSDs of the New Low Noise Model (NLNM) [46] and the measured former noise [47], and the noise is consitent with the NLNM between 2 Hz and 30 mHz. Moreover, the latter noise is increase PSD increases rapidly with decreasing frequency below 2 mHz. ここで特筆すべきは、2mHz 以上のノイズは Rayleigh wave で運ばれるため、地下に潜ればいくらか低減が期待されることである。実際に地表と地下のひずみ計による観測によってそれが示唆されている [53]。

Earth tides

Below more lower frequency, the earth deformed by tidal forces due to the attraction of the Sun and the Moon in diurnal and semi-diurnal period.

(なにかもう少し書く)

Large Earthquake in the world

大規模な地震ほど低周波の地面振動成分が卓越することが知られている [54, 55]。地震によるサイトの地面振動は断層のズレ方と伝搬経路に依存するが、ここでは、

同じ場所で同じ震源同じ断層のズレ方を前提とする。このとき以下のようなモデルが観測値をよく説明する。

$$s(\omega) = \frac{S_0}{1 + (\omega/\omega_0)^2} \quad (1.29)$$

ここで M_s は表面波マグニチュードである [56]。そして S_0 は M_s に比例した定数で、 ω_0 は $M_s^{1/3}$ に比例したコーナー周波数である。この変位スペクトルをさまざまな表面波マグニチュードでプロットしたものを Fig(??) に示す。

このように大規模地震は低周波の地面振動を励起しやすく、特に

1.3 Study of Seismic Noise of KAGRA Mine

1.3.1 Overview

KAGRA では、我々は地面振動を地震計とひずみ計をつかったリアルタイムモニターシステムを構築している。このシステムの目的は、地面振動に最も敏感な腕共振器を懸架する TypeA サスペンションの地面振動をモニターすることである。そのため、我々は広帯域地震計である Trillium120 を 3 台、TypeA が懸架されているコーナーエリアと両エンドエリアの二階の地面に設置し、ひずみ計は現在 X アームに設置している。これらセンサーは自身のセンサーノイズの特性上、帯域を相補的に地面振動をモニターしている；0.1Hz 以上は地震計で、1Hz 以下はひずみ計でモニターしている。

本節ではこれらセンサーをつかって、KAGRA の地面振動ノイズの時間的空間的な特徴を調べた。

1.3.2 Experimental Arrangement

We used Trillium 120-QA which is known as three-component, very broadband, and low-noise seismometer. These three outputs are proportional to the ground velocity of two horizontal and one vertical, respectively.

The seismometer is housed in the black thermal insulation cover as shown in fig 1.6. Thermal insulation protects two broad categories of thermal couplings that can cause unwanted noise [57]. First is the direct coupling to the sensitivity.



Figure 1.6: Trillium 120-QA installed on the second floor at X-end area, which is covered by black thermal insulation cover

This coupling typically increases the noise of the vertical channel as a periodic diurnal variation caused by the day-to-night temperature cycle, because the springs that suspended the inertial masses are temperature sensitive. The second is the coupling to tilt from the thermal fluctuation. Tilt converts the vertical acceleration of gravity into horizontal acceleration. This thermally induced tilt noise on the horizontal will be larger than the direct thermal coupling on the vertical channel. To be low sensitivity to both tilt and temperature, this model has a function to center the inertial mass after the initial installation.

The signals of the seismometer is recorded through the data acquisition system developed by LIGO [58]. The analog signal is converted to digital signal by the 16 bit analog-to-digital converters (ADC) with 16384 Hz sampling. This analog signal is amplified with 30 db so that the ADC noise does not mask this signal.

1.3.3 Data Processing

振幅スペクトルの推定は 50%オーバーラップした 32 個のセグメントの平均で得た。それぞれのセグメントの FFT の計算は、まず dtrend をして線形成分を取り除き、Hanning 窓にかけてから行った。32 回の平均をおこなったスペクトルは自由度 32 のカイ二乗分布に従う。自由度 ν のときの $100(1 - \alpha)\%$ の信頼区間は、周

波数 f でのスペクトルの推定量を $\hat{G}(f)$ とすると、

$$\frac{\nu \hat{G}(f)}{\chi^2(\nu, 1 - \frac{\alpha}{2})} \leq G(f) \leq \frac{\nu \hat{G}(f)}{\chi^2(\nu, \frac{\alpha}{2})} \quad (1.30)$$

で与えられる。したがって、95%の信頼区間は

$$\nu / \chi^2(\nu, 1 - \frac{\alpha}{2}) \leq G(f) / \hat{G}(f) \leq \nu / \chi^2(\nu, \frac{\alpha}{2}) \quad (1.31)$$

となり、自由度 32 の場合、推定量の 0.65 から 1.75 の範囲になる。

1.3.4 Study of Long-term Seismic Noise

Long-term seismic noise is measured by a seismometer installed on the second floor of the X-end area. This area is placed 200 m underground from the surface of the mountain. In comparison to corner area, human activity in the end area is less because the corner area has parking lots. In comparison to the Y-end area, there is no entrance connected to other mines. Therefore, the X-end area is relatively quiet in the KAGRA mine, regarding the seismic noise induced by human activity.

地震や回路からの突発的なノイズを含まない一年間のデータをつかって、ノイズスペクトルを計算した。並進成分と垂直成分両方の加速度の ASD を Figure 1.7 に示す。40mHz 以上では並進成分も垂直成分も同じ振幅スペクトル密度をもつ。40mHz 以下で並進成分が垂直成分よりも大きい、これは付録で後述しているとおり、無相関なノイズである。おそらく温度ゆらぎから生じる傾斜カップリングだと考えられる。また、Peterson のスペクトルと測定で得た 10 パーセントイルを比較すると、0.1 から 2Hz をのぞいて、NLNM と同じである。0.1Hz 以下では垂直成分は地面振動のノイズレベルと同等であり。2Hz 以上は、並進も垂直成分も、地下環境のおかげで静かである。対照的に 0.1 から 2Hz の帯域では、並進成分も垂直成分も NLNM より数倍大きい。これは KAGRA が富山湾から 40km の距離にあり、比較的脈動の影響を受けやすいためと考えられる。

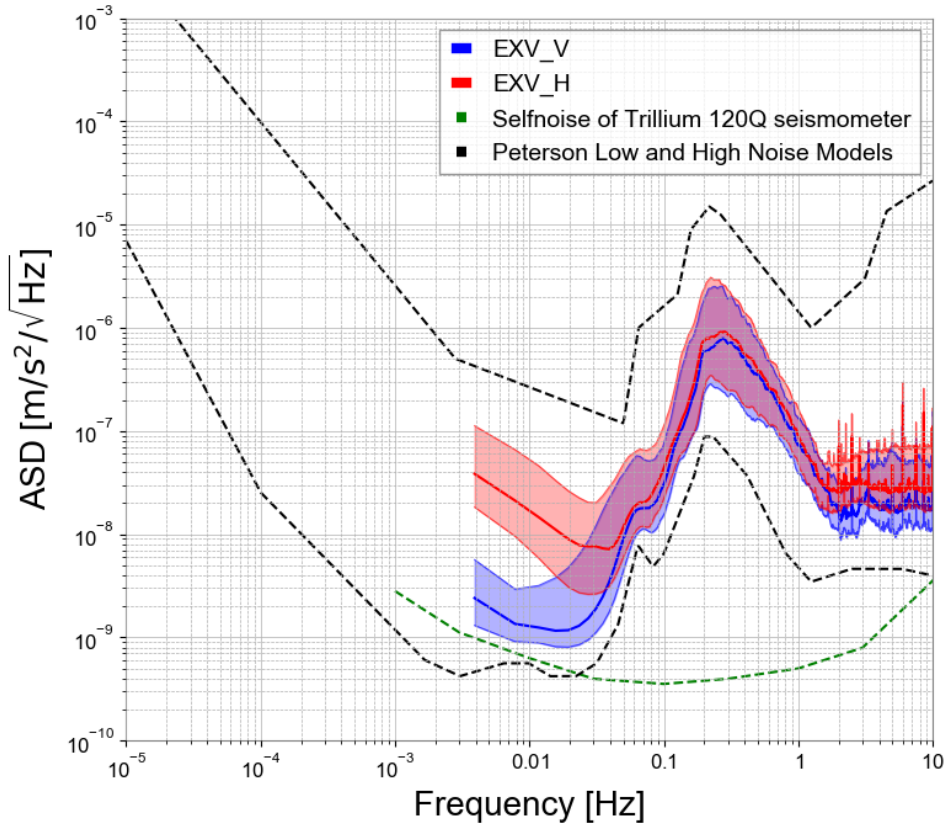


Figure 1.7: 赤の実線は垂直成分の 50 パーセンタイルで、下と上に 10 と 90 パーセンタイルを示す。青の実線は X 軸と Y 軸の二乗和から求めた並進成分であり、同様に 10,50,90 パーセンタイルを示す。緑点線は Trillium120 のデータシートから引用した Selfnoise である。黒の点線は Peterson の NLNM と NHNM である。

1.3.5 Study of the Differential Motion Reduction

CDMR in X-arm

1.1.2 でのべた CDMR の効果を, X アームの両端においた地震計 2 台をつかって評価した。

基線長の違いによる CDMR の変化

aaa

1.4 Summary of the Chapter

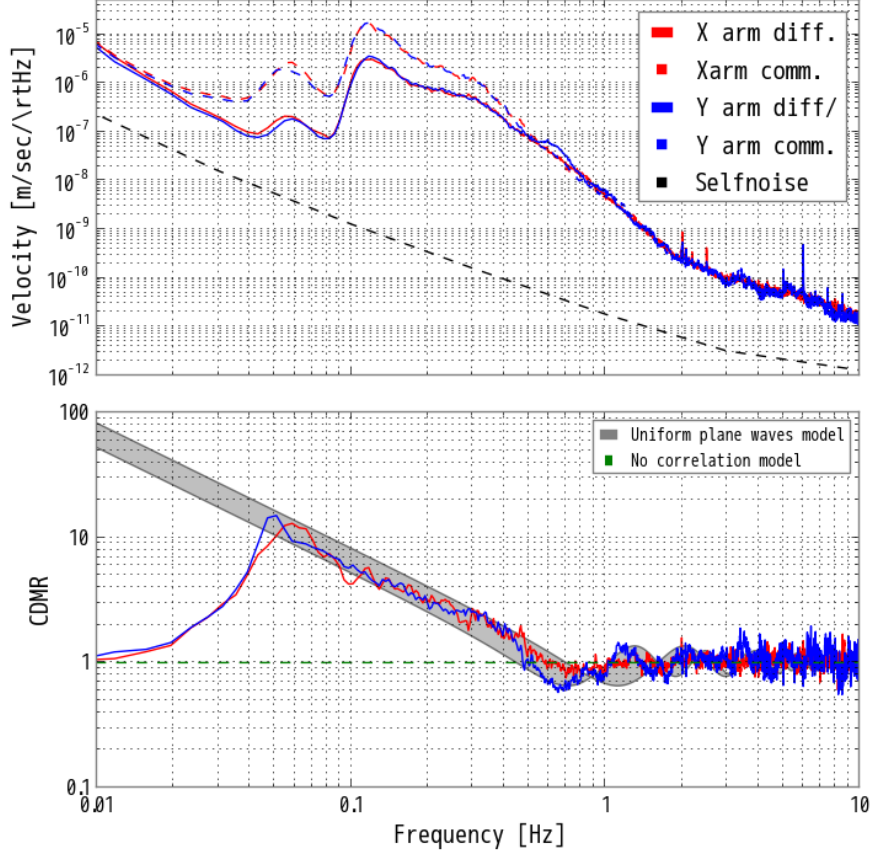
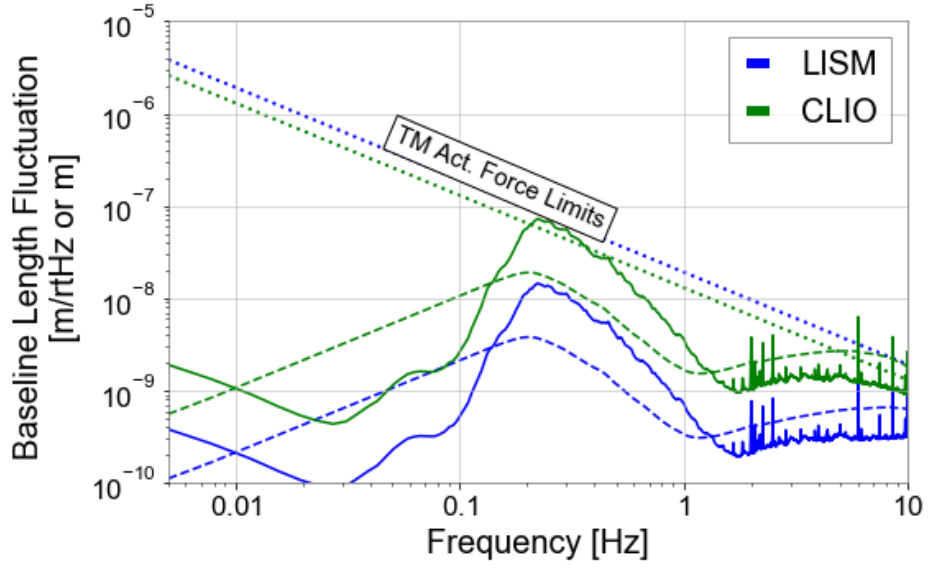
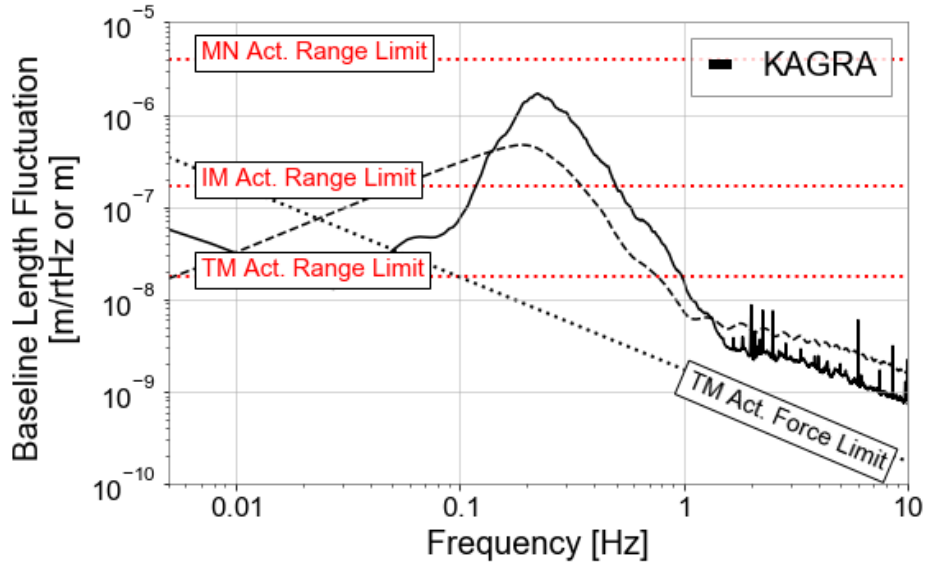


Figure 1.8: Comparison with the measured CDMR and the uniform plane waves model. (Top) ASDs of the velocity of the differential (solid line) and common motion (dashed line) of the baseline used calculating the below CDMR. Red and blue indicate X-arm and Y-arm, respectively. As a comparison to these ASDs, black dashed line shows the selfnoise of the Trillium 120Q broadband seismometer multiplied $\sqrt{2}$. Below 0.05 Hz, the ASDs are limited by the noise mentioned in section 1.3.2. (Bottom) The CDMR of the baseline calculated with the differential and common motion of the baseline according to the definition in Eq.(1.16). Gray line indicates the CDMR assuming the uniform plane waves model in case the phase velocity is in region from 5 – 3 km/sec. Green dashed line is the CDMR assuming the no correlation between the each end points of the baseline. The measured CDMR is consistent with the uniform model in 0.05 – 0.5 Hz. Below this band, the CDMR is close to the no correlation model due to the noise of the seismometers. Above this band,



(a)



- (b) Comparison between the baseline length fluctuations and the displacement requirement of the underground GW detectors. Solid line is the baseline length fluctuation of the detectors, which is the ASD of the seismic noise (described in section 1.3) multiplied by the function in Eq. ?? assuming the uniform plane wave model with the phase velocity of 3 km/sec. Moreover, dashed line is the accumulated RMS of the fluctuations. As a comparison, the displacement requirement of the detector, which is the linewidth of the arm cavity, is plotted.

Figure 1.9: aa

Table 1.2: Comparison of the underground GW detectors

Detector	Baseline length [m]	Linewidth [μm]
LISM	20	0.1
CLIO	100	0.1

Bibliography

- [1] Shuichi Sato, Shinji Miyoki, Souichi Telada, Daisuke Tatsumi, Akito Araya, Masatake Ohashi, Yoji Totsuka, Mitsuhiro Fukushima, Masa-Katsu Fujimoto, LISM Collaboration, et al. Ultrastable performance of an underground-based laser interferometer observatory for gravitational waves. *Physical Review D*, 69(10):102005, 2004.
- [2] M Punturo, M Abernathy, F Acernese, B Allen, Nils Andersson, K Arun, F Barone, B Barr, M Barsuglia, M Beker, et al. The einstein telescope: a third-generation gravitational wave observatory. *Classical and Quantum Gravity*, 27(19):194002, 2010.
- [3] B P Abbott, R Abbott, T D Abbott, M R Abernathy, K Ackley, C Adams, P Addesso, R X Adhikari, V B Adya, C Affeldt, et al. Exploring the sensitivity of next generation gravitational wave detectors. *Class. Quantum Grav*, 34(044001):044001, 2017.
- [4] L Naticchioni, M Perciballi, F Ricci, E Coccia, V Malvezzi, F Acernese, F Barone, G Giordano, R Romano, M Punturo, et al. Microseismic studies of an underground site for a new interferometric gravitational wave detector. *Classical and Quantum Gravity*, 31(10):105016, 2014.
- [5] 西村太志 長谷川昭, 佐藤春夫. *Seismology*, volume 6 of *Introduction to Modern Earth Science Series*. Kyoritsu.
- [6] 竹本修三, 新谷昌人, 赤松純平, 森井互, 東敏博, 福田洋一, 尾上謙介, 市川信夫, 川崎一朗, 大橋正健, et al. 神岡鉱山における 100 メートルレーザー伸縮計について. 2003.

- [7] Sylvette Bonnefoy-Claudet, Fabrice Cotton, and Pierre-Yves Bard. The nature of noise wavefield and its applications for site effects studies: A literature review. *Earth-Science Reviews*, 79(3-4):205–227, 2006.
- [8]
- [9] M G Beker, J F J van den Brand, E Hennes, and D S Rabeling. Newtonian noise and ambient ground motion for gravitational wave detectors. *Journal of Physics: Conference Series*, 363:012004, jun 2012.
- [10] R. Schofield et al. Source and propagation of the predominant 1-50 hz seismic signal from off-site at ligo-hanford. In LIGO Scientific Collaboration Meeting, Hanford, August 2000.
- [11] F Acernese, P Amico, N Arnaud, D Babusci, R Barillé, F Barone, L Barsotti, M Barsuglia, F Beauville, MA Bizouard, et al. Properties of seismic noise at the virgo site. *Classical and Quantum Gravity*, 21(5):S433, 2004.
- [12] Jon R Peterson. Observations and modeling of seismic background noise. Technical report, US Geological Survey, 1993.
- [13] Kiwamu Nishida, Naoki Kobayashi, and Yoshio Fukao. Origin of earth’s ground noise from 2 to 20 mhz. *Geophysical Research Letters*, 29(10):52–1, 2002.
- [14] P Bormann. New manual of seismological observatory practice. *GFZ German Research Centre for Geosciences*, 2012. [Link](#).
- [15] RA Haubrich, WH Munk, and FE Snodgrass. Comparative spectra of microseisms and swell. *Bulletin of the Seismological Society of America*, 53(1):27–37, 1963. [Link](#).
- [16] Michael Selwyn Longuet-Higgins. A theory of the origin of microseisms. *Philosophical Transactions of the Royal Society of London. Series A, Mathematical and Physical Sciences*, 243(857):1–35, 1950. [Link](#).

- [17] GG Sorrells, John A McDonald, ZA Der, and Eugene Herrin. Earth motion caused by local atmospheric pressure changes. *Geophysical Journal International*, 26(1-4):83–98, 1971.
- [18] W Zürn and R Widmer. On noise reduction in vertical seismic records below 2 mhz using local barometric pressure. *Geophysical Research Letters*, 22(24):3537–3540, 1995.
- [19] A ARAYA. Broadband observation with laser strainmeters and a strategy for high resolution long-term strain observation based on quantum standard. *J. Geod. Soc. Japan*, 53:81–97, 2007.
- [20] Keiiti Aki and Paul G Richards. *Quantitative seismology*. 2002.
- [21] Keiiti Aki. Scaling law of seismic spectrum. *Journal of geophysical research*, 72(4):1217–1231, 1967.
- [22] B. Gutenberg. Amplitudes of surface waves and magnitudes of shallow earthquakes*. *Bulletin of the Seismological Society of America*, 35(1):3–12, 01 1945.
- [23] Nanometrics Inc., 250 Herzberg Road Kanata, Ontario, Canada K2K 2A1. *Trillium 120Q/QA User Guide*, 04 2017.
- [24] Rolf Bork, R Abbott, D Barker, and J Heefner. An overview of the ligo control and data acquisition system. *arXiv preprint physics/0111077*, 2001.